Journal of Materials Chemistry A

ROYAL SOCIETY OF CHEMISTRY

PAPER

View Article Online
View Journal

Cite this: DOI: 10.1039/d6ta01576j

Electrochemo-mechanical coupled behaviors in sodium-ion batteries upon stack pressure

Bo Rui,[ab] Youngwon Hahn,[c] Amit Bhowmick,[ab] Farzaneh Mousavi,[c] Sandeep Kulathu,[c] Victor Oancea[c] and Jun Xu *[abd]

Owing to their low cost, environmental friendliness, and high safety, sodium-ion batteries (SIBs) are considered promising alternatives to lithium-ion batteries (LIBs). However, the electrochemo-mechanical coupled behaviors of sodium-ion batteries, which represent a typical and critical operational scenario, remain largely unexplored. In this study, a unique bimodal swelling behavior specific to sodium-ion batteries is revealed through *operando* swelling-force measurements upon stack pressure. Meanwhile, a detailed, multiscale electrochemo-mechanical computational framework, rigorously validated by experiments, is developed to quantitatively assess the contributions of individual cell components to the overall swelling behavior. The results show that swelling is primarily driven by anode expansion at low state-of-charge (SOC), whereas cathode-driven shrinkage governs swelling at high SOC, with the separator serving mainly as a load-transfer and mechanical-buffering layer. In addition, an SOC-dependent, electrode-dominated swelling mechanism for sodium-ion batteries is systematically established and elucidated. Finally, higher C-rates lead to higher swelling force at full charge and an earlier peak force during discharge. Overall, this study provides fundamental insights into electrochemo-mechanical coupling in sodium-ion batteries and offers important guidance for the development of safer next-generation sodium-ion battery systems.

Received 22nd February 2026
Accepted 17th April 2026

DOI: 10.1039/d6ta01576j

rsc.li/materials-a

1 Introduction

Sodium-ion batteries (SIBs) have gained widespread attention owing to their abundant raw materials,[1] low cost,[2–4] environmental sustainability[5,6] and high safety,[6,7] making them an ideal alternative[8] to lithium-ion batteries (LIBs) with strong potential for large-scale energy storage systems and electric vehicles (EVs). In real-world application scenarios, battery operation involves complex multiphysics behaviors, including electrochemical processes (*e.g.*, fast charging[9]), mechanical effects (*e.g.*, stack pressure[10]), and thermal influences (*e.g.*, extreme ambient temperatures[11]), which are strongly coupled.[12,13] Swelling behavior represents a typical electrochemo-mechanical coupled phenomenon[14] that has an impact on externally applied mechanical constraints during module or pack assembly or on efforts to enhance interfacial contact, particularly in solid-state batteries (SSBs).[15]

Swelling behavior in batteries primarily originates from particle-level volume expansion during charge and discharge,[16–20] and existing studies have predominantly focused on lithium-ion batteries (LIBs). At the particle scale, lithium ions intercalate into small-deformation electrode materials such as graphite,[20–22] or undergo alloying reactions with large-deformation materials such as silicon,[23–25] leading to significant volumetric expansion[23] up to 300%. In addition, in conversion-type sulfur cathodes, the reversible conversion between S and Li_2S/Li_2S_2 during cycling is accompanied by significant phase transformation and morphology evolution, leading to substantial volume change.[26–28] This expansion, which induces localized stress,[18,23] may lead to particle cracking or fracture.[20,23] At the electrode scale, particle swelling reduces electrode porosity[29,30] and causes overall electrode expansion,[19,31–33] thereby altering key electrochemical transport properties, including tortuosity,[34,35] electronic and ionic conductivity,[36,37] and effective diffusion coefficients.[38,39] At the cell scale, encompassing pouch cells,[19] prismatic cells,[40–42] and cylindrical 18 650 cells,[43–45] swollen electrodes deform in conjunction with the separator. Under unconstrained conditions,[21,46] this manifests as macroscopic cell swelling and displacement,[47] whereas upon mechanical constraints,[48,49] it results in the development of macroscopic swelling force or stack pressure.[50,51] Typical swelling behavior in lithium-ion batteries is characterized by a monotonic increase in swelling force during charging and a decrease during discharging,[52,53] which is primarily attributed to volumetric expansion of the

[a]Department of Mechanical Engineering, University of Delaware, Newark, DE, 19716, USA. E-mail: junxu@udel.edu
[b]Energy Mechanics and Sustainability Laboratory (EMSLab), University of Delaware, Newark, DE, 19716, USA
[c]Dassault Systèmes Americas Corp., 1301 Atwood Ave, Suite 101W, Johnston, RI, 02919, USA
[d]Data Science Institute, University of Delaware, Newark, DE, 19716, USA

anode,[54,55] such as graphite. Although cathode materials also undergo volume changes, their contributions are generally smaller, as observed in LCO[21] and NMC.[56] An important exception is the LFP/graphite system,[57] which exhibits non-monotonic swelling behavior during charge and discharge due to the relatively large volume change of the LFP cathode. Furthermore, the application of mechanical constraint has been shown to significantly enhance battery cycle life,[58] mainly by suppressing parasitic side reactions such as lithium plating and excessive solid electrolyte interphase (SEI) growth.

Research on swelling behavior in SIBs remains relatively limited. Atomistic simulations have shown that lattice strain developed during charge and discharge can significantly affect ion transport,[59] as demonstrated in olivine phosphate cathodes such as $NaFePO_4$. Conversely, the magnitude of swelling strain is influenced by the cycling rate and the growth of the cathode electrolyte interphase (CEI),[60] as observed in sodium iron phosphate systems. These findings highlight the strong coupling between mechanical and electrochemical processes in sodium-ion batteries.[60] In addition, electrodes exhibit pronounced irreversible mechanical deformation during cycling,[61] which is primarily attributed to irreversible CEI formation, for example, in sodium chromium oxide ($NaCrO_2$) cathodes.

However, the swelling behavior of sodium-ion batteries and the underlying mechanisms remain poorly understood, underscoring the urgent need for systematic investigation. To bridge this gap, this study focuses on elucidating the electrochemo-mechanically coupled swelling behavior of sodium-ion batteries and their underlying mechanisms. *Operando* swelling-force measurements are employed to reveal the swelling behavior, while a detailed, experimentally validated multiscale electrochemo-mechanical coupled computational framework is used to interpret the origins of the swelling force and to quantify the contributions of individual components. In addition, an SOC-dependent, electrode-dominated swelling mechanism is established. Finally, the influence of C-rate on swelling behavior is systematically investigated.

2 Methodology

2.1 *Operando* swelling force measurement setup

Charge–discharge tests under mechanical constraints were performed to investigate the electrochemo-mechanically coupled swelling behavior of sodium-ion batteries. The charge–discharge testing system consisted of a battery cycler (Neware CT-4008), a temperature chamber (Neware WHW-200), and a data acquisition unit for electrochemical measurements (Fig. 1a). For mechanical measurements, a high-precision swelling force measurement fixture (InnCise, 5000 N capacity) was employed to continuously monitor the evolution of swelling force in real time. An initial preload of approximately 125 N was applied to the cell to eliminate initial surface nonuniformity (Fig. 1b).

In this study, a commercially manufactured $Na_{0.97}Ca_{0.03}[Mn_{0.39}Fe_{0.31}Ni_{0.22}Zn_{0.08}]O_2$ layered oxide (NNMF)/hard carbon (HC) electrolyte-free sodium-ion pouch cell (LiFUN) was employed (Fig. 1b). The tested pouch cell had dimensions of 30 mm × 18.2 mm × 5.6 mm. 1 m $NaPF_6$ in a propylene carbonate/ethyl methyl carbonate (PC : EMC = 1 : 1 by volume) mixture, with the addition of 2% fluoroethylene carbonate (FEC) is used as

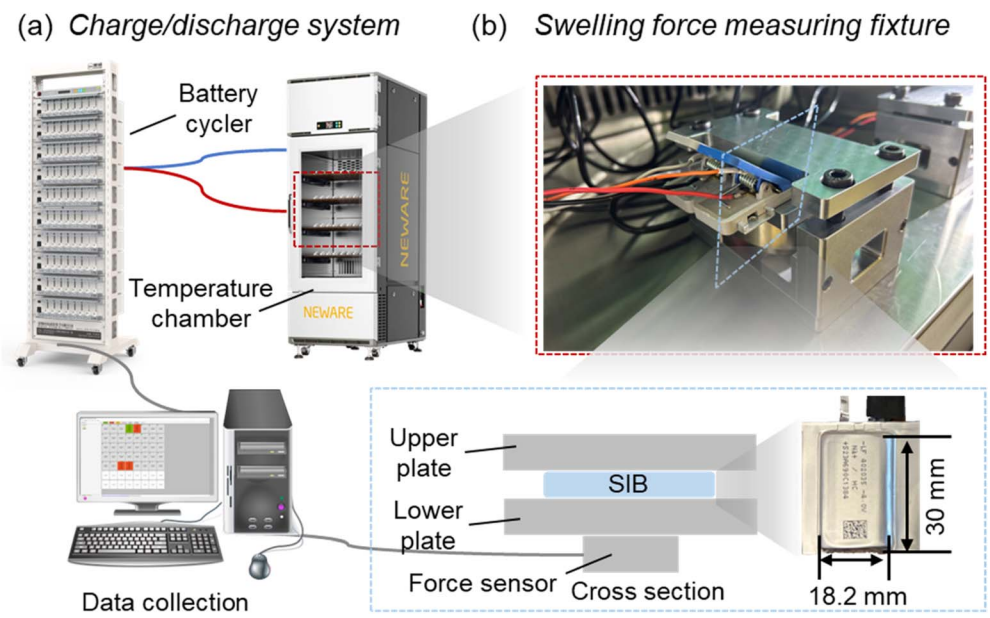

Fig. 1 Experimental setup for operando swelling force measurement of sodium-ion batteries (SIBs). (a) Integrated charge–discharge and thermal control system, consisting of a battery cycler, a temperature chamber, and a data acquisition unit for synchronized electrochemical and mechanical measurements. (b) Swelling force measuring fixture placed inside the temperature chamber. The fixture applies a controlled through-thickness constraint to the cell while enabling real-time force sensing during cycling. The lower schematics illustrate the cross-sectional configuration of the fixture, including the upper and lower plates and the force sensor, with the SIB sandwiched between the rigid plates. The cell dimensions are 18.2 mm × 30 mm, as indicated.

Table 1 Basic information about sodium ion battery

Parameters	Value
Theoretical capacity	220 mA h
Reversible capacity	~200 mA h
Charging cutoff voltage	4.0 V
Discharging cutoff voltage	1.5 V
Cathode active material	NNMF
Anode active material	HC
Cathode & anode current collector	Al
Casing	Al plastic film
Layer number	14

electrolyte. After adding the electrolyte, the batteries were sealed using a Vacuum Sealer (MASK-115-III) in an argon-filled glove box (Vigor SG2400/750TS, H_2O < 0.1 ppm, O_2 < 0.1 ppm). The cell was rested for 12 hours to ensure sufficient electrolyte infiltration of the jellyroll. The cell underwent three formation cycles at 0.1C using a charge–discharge instrument (Neware CT-4008) under 25 °C and an applied pressure of 0.1 MPa. After formation, the cell was degassed and subsequently resealed. The cell ultimately exhibited a reversible capacity of approximately 200 mA h. The cathode and anode used in this work had areal mass loadings of 16.0 mg cm^{-2} and 9.55 mg cm^{-2}, respectively. Their compacted densities were 2.9 g cm^{-3} for the cathode and 0.8 g cm^{-3} for the anode. Considering the active-material fractions of 95.2 wt% for the cathode and 95.5 wt% for the anode, together with the corresponding specific capacities of 140 mA h g^{-1} and 280 mA h g^{-1}, the estimated areal capacities were approximately 2.13 mA h cm^{-2} and 2.55 mA h cm^{-2}, respectively. The resulting N/P ratio, based on areal capacity, was approximately 1.20. The operating voltage window was set to 1.5–4.0 V. The jellyroll, encapsulated in an aluminum-plastic laminate pouch, consisted of 14 repeating units, each comprising one cathode layer, one anode layer, and two separator layers (Table 1). The cathodes and anodes adopt sandwich architectures, with active material coated on both sides of the current collectors (see Table 1 for details).

2.2 Electrochemo-mechanical computational framework

A detailed three-dimensional (3D) computational framework for sodium-ion batteries was developed in ABAQUS[62] to systematically elucidate the mechanisms underlying electrochemo–mechanical coupled swelling behavior. Consistent with the actual cell architecture, a total of 14 repeating units were constructed, comprising 14 cathode layers, 15 anode layers, and 30 separator layers. Each cathode and anode layer consisted of one current collector and two active material layers, and the tabs were also explicitly included to accurately represent the cell structure (Fig. 2a). The geometric parameters of the model are listed in Table S1.

The computational framework employs porous electrode theory (PET),[63–65] which predicts electrochemical behavior using a homogenized porous electrode representation with a fully coupled three-dimensional macroscale electrode framework

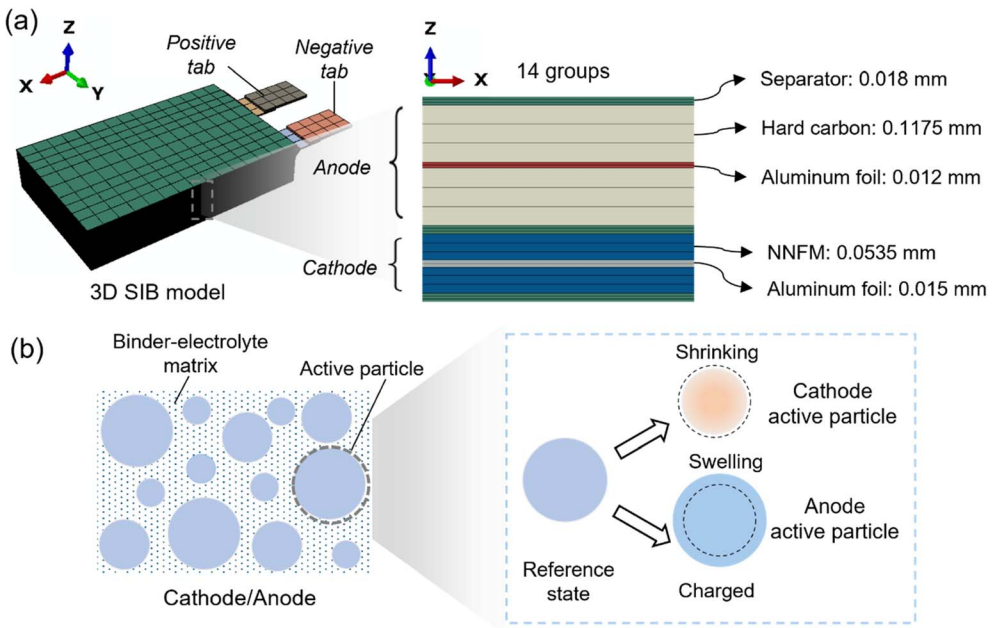

Fig. 2 Electrochemo-mechanical computational framework for sodium-ion batteries (SIBs). (a) Three-dimensional stacked SIB model and detailed layer configuration along the thickness (z) direction. The model consists of 14 repeated electrode–separator groups, including a separator (0.018 mm), an active material (NNFM, 0.0535 mm), an aluminum current collector (0.015 mm), a HC anode (0.1175 mm), and an aluminum foil (0.012 mm). Positive and negative tabs are explicitly represented, and the global coordinate system is indicated. (b) Schematic illustration of the mesoscale electrode microstructure and particle-level deformation mechanisms. Active particles are mixed with a binder–electrolyte matrix for both the cathode and the anode. During electrochemical cycling, cathode active particles undergo volumetric shrinkage upon charging, whereas anode active particles experience pronounced swelling, giving rise to heterogeneous internal stress evolution at the particle scale.

and a one-dimensional microscale particle framework (pseudo-4D formulation, P4D).[66] The classical porous-electrode theory is not elaborated here; instead, the focus is on describing the coupling between the mechanical and electrochemical components. During charge and discharge, sodium ions intercalate into and deintercalate from the active particles, leading to particle expansion and contraction, *i.e.*, diffusion-induced strain at the particle scale. As an example, sodium ions deintercalate from NNMF particles and intercalate into HC particles, leading to cathode particle shrinkage and anode particle expansion (Fig. 2b).

Particle expansion induces variations in porosity. The porous mechanics formulation simplifies the active particles and binder into an equivalent homogeneous solid phase (grains) to account for their combined mechanical effects (eqn (1)–(3)).[66] This treatment captures the influence of mechanical deformation on electrochemical behavior.

$$J_g = \frac{\varphi^{p}_{total} + e^{b}_{0}}{1 + e^{b}_{0}} \tag{1}$$

$$\varphi^{p}_{total} \overset{def}{=} \frac{\sum_i V^{P_i}}{\sum_i V^{P_i}\Big|_{t=0}} = \sum_i \theta^{P_i} \varepsilon^{p_i}. \tag{2}$$

$$\theta^{P_i} = \frac{J^{P_i}}{J^{P_i}\Big|_{t=0}} = \frac{V^{P_i}}{V^{P_i}|_{t=0}} \tag{3}$$

where J_g is used to update the porosity and the total volume fraction, e^{b}_{0} denotes the initial volume ratio of the binder to the active particles, and φ^{p}_{total} represents the total accumulated particle expansion. Here, $\theta^{P}{}_{i}$ denotes the volumetric expansion of a given particle, representing the ratio of the particle volume to its initial volume, $\varepsilon^{P}{}_{i}$ is the initial volume fraction of that particle within the electrode, and $V^{P}{}_{i}$represents the particle volume at the current time. Since only one type of active particle is present in both the cathode and anode in this study, $i = 1$. Particle expansion leads to overall electrode swelling, which is described by an effective eigenstrain tensor. The collective expansion of the grains is converted into an average radial elongation, which is assumed to be isotropic linear expansion.

$$\bar{\lambda}^{p}_{r} \overset{def}{=} (J_g)^{\frac{1}{3}} \tag{4}$$

where $\bar{\lambda}^{p}_{r}$ denotes the average radial stretch, λ_α represents the electrode stretch along the principal directions ($\alpha = 1, 2, 3$). Subsequently, $\bar{\lambda}^{p}_{r}$ is introduced to further characterize the electrode elongation along different directions.

$$\lambda_\alpha = (\bar{\lambda}^{p}_{r})^{S_\alpha} \tag{5}$$

where S_α is a configuration parameter that governs the transfer of microscopic expansion to the macroscopic electrode skeleton and depends on the electrode geometry, primarily reflecting the macroscopic electrode's anisotropic swelling. Finally, the principal logarithmic strains are taken as the final skeleton principal eigenstrains.

$$\varepsilon^{eig}_{\alpha} = \log \lambda_\alpha = S_\alpha \log \bar{\lambda}^{p}_{r} \tag{6}$$

The influence of internal stress on electrochemical behavior is not pronounced[12] and is therefore neglected in this study to improve computational efficiency. At the macroscale, the model accounts for Butler–Volmer reaction kinetics at the electrode particle surface, ensuring charge and ion conservation. At the microscale, ion transport within active particles is described by Fick's diffusion laws.

Based on our previous work,[7] tensile responses on both cathode and anode materials do not exhibit pronounced plastic deformation. Therefore, linear elastic constitutive models are adopted for both electrode materials. In addition, although the separator exhibits clear mechanical anisotropy, battery swelling is predominantly governed by thickness-directional deformation rather than in-plane deformation. Accordingly, a linear elastic constitutive model is also employed for the separator. The material parameters and governing equations of the computational framework are summarized in Tables S2 and S3. Both the 1D and 3D frameworks show good agreement with the experimental data, demonstrating the model's predictive accuracy (Fig. 3 and S1).

Although the pressure response analyzed in this work is presented at the pouch-cell scale, its origin lies in particle-level electrochemical and chemo-mechanical processes within the electrode materials. In particular, sodium insertion/extraction induces composition-dependent eigenstrain in active particles, and these local material deformations are transmitted through the porous electrode architecture and external mechanical constraint to produce electrode thickness evolution, stress redistribution, and macroscopic swelling force. Therefore, the cell-level pressure behavior is not treated here as a purely phenomenological response, but as the cumulative consequence of material-chemistry-dependent deformation at the particle scale.

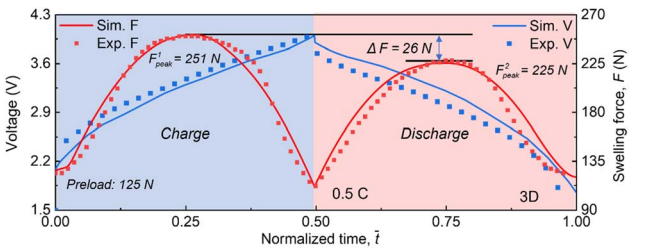

Fig. 3 Bimodal electrochemo–mechanical coupled swelling behavior and model validation of sodium-ion batteries. Coupled voltage and swelling force responses under 0.5C cycling with an initial preload of 125 N. The shaded regions denote charge (in blue) and discharge (in pink) stages. Solid lines represent simulation predictions, while symbols correspond to experimental data. The simulation model accurately reproduces both the voltage evolution and the swelling force dynamics, including the peak swelling forces during charge (F^{1}_{Peak} = 251 N) and discharge (F^{2}_{Peak} = 225 N), as well as the force difference ΔF = 26 N, validating the predictive capability of the coupled electrochemo-mechanical framework. Here, normalization is performed using the full-cycle duration at the corresponding C-rate.

3 Electrochemo-mechanical origin of cell swelling

3.1 Bimodal electrochemo–mechanical coupled swelling behavior

Applying stack pressure during cell charge and discharge represents a typical electrochemo-mechanically coupled boundary condition[10] (Fig. 1b). During charging, the cell voltage increases from 1.5 to 4.0 V. Upon the transition from charging to discharging, a small voltage drop occurs due to the internal resistance of the cell. At the end of discharge, the voltage returns to 1.5 V. As charging proceeds, the swelling force increases and reaches its first peak of 251 N at a normalized time of 0.25 (50% SOC). At this point, the voltage increases to 3.38 V. With continued charging, the swelling force counterintuitively decreases to approximately 112 N at full charge (100% SOC, 4 V), slightly lower than the applied preload of 125 N. This reduction is likely attributable to stress relaxation within the cell.[19] During the subsequent discharge, the swelling-force evolution follows a similar trend to that observed during charging, but with a lower peak value $F^2_{\mathrm{Peak}} = 225$ N at around 3 V, *i.e.*, $\Delta F = 26$ N lower than F^1_{Peak} (Fig. 3). The concurrent variations in cell voltage and swelling force provide direct evidence of electrochemo-mechanical coupling.

To further connect the measured cell-level swelling response with electrode chemistry, we note that prior *operando*/*in situ* studies on hard-carbon anodes have shown sodium-storage behavior that evolves from defect/surface adsorption to interlayer insertion and nanopore filling, together with measurable stress generation during sodiation.[67–69] In parallel, layered sodium transition-metal oxide cathodes exhibit SOC-dependent phase evolution and lattice-parameter changes during Na extraction/insertion, which can produce non-monotonic dimensional changes.[70,71] Therefore, the macroscopic swelling observed here is consistent with the coupled contribution of HC expansion and layered-oxide structural evolution under mechanical constraint.

This distinctive bimodal swelling behavior represents a characteristic electrochemo-mechanically coupled response in NNMF sodium-ion batteries. To further elucidate the underlying mechanisms and quantify the contributions of individual components to the overall swelling behavior, a validated multiphysics computational framework is employed in the following analysis (Fig. 3).

To further examine the stability and reproducibility of the swelling-force response, additional cycling measurements were conducted under different rates and preloading conditions. Under a preload force of 45 N and a current of 10 mA, the swelling-force signal exhibits stable periodicity across repeated cycles and remains closely correlated with the corresponding voltage profile (Fig. S2). These results further confirm the robustness and reproducibility of the characteristic swelling-force behavior, including the bimodal feature observed during cycling.

3.2 Component-wise analysis of swelling contributions

During a charging process from 0% to 100% SOC, sodium ions deintercalated from the cathode, causing the cathode particles to undergo approximately 10.0% volumetric shrinkage (Fig. S3), ultimately resulting in approximately 3.2% shrinkage in the through-thickness direction (Fig. 4a). At the anode, sodium ions intercalate into the active particles, leading to a volumetric expansion of approximately 4.4% (Fig. S2) and an approximately 1.4% expansion of the anode in the through-thickness direction (Fig. 4a). The cathode and anode therefore exhibit competing thickness evolutions. In terms of eigenstrain rate, the cathode eigenstrain rate $\dot{\varepsilon}^{\mathrm{eig}}$ generally decreases rapidly, except for a slight increase at SOC below 5%. While charging, the cathode $\dot{\varepsilon}^{\mathrm{eig}}$ is negative, indicating that the shrinkage rate of the cathode is continuously increasing. In contrast, although the anode $\dot{\varepsilon}^{\mathrm{eig}}$ remains positive, it exhibits only minor fluctuations at low SOC (0–50%) and then decreases rapidly at high SOC (50–100%) (Fig. 4b). Even though the anode expansion rate is smaller in magnitude than the cathode shrinkage rate, the anode has a larger thickness, so its net through-thickness contribution dominates the swelling response in the low-SOC regime. Consistently, the cell-level swelling force increases in this range (Fig. 3). At high SOC, the cathode shrinkage rate continues to increase while the anode expansion rate diminishes (Fig. 4b), leading to a transition to cathode-shrinkage-dominated behavior and a corresponding decrease in swelling force (Fig. 3). This transition explains the emergence of a swelling-force peak near 50% SOC. The discharge process exhibits a similar trend. Overall, the bimodal swelling behavior originates from the competing expansion–shrinkage mechanisms between the anode and cathode in sodium-ion batteries.

To quantify the contributions of the cathode and anode to the overall swelling force, we first conducted simplified simulations in which the computational framework selectively activated either anode expansion or cathode shrinkage. However, because the separator acts as a compliant buffer layer, its mechanical response varies across cases, complicating the interpretation of single-electrode behavior. Notably, the separator itself does not generate swelling force; it serves solely as a load-transfer medium. We therefore quantify the cathode and anode contributions to the measured stack force by attributing the boundary reaction force to electrode eigenstrain sources using Shapley decomposition.[72] This approach ensures strict additivity of contributions, even under strong mechanical coupling and nonlinear interactions among cell components. Under the same external constraint, when only anode expansion is considered, a positive reaction force is obtained that increases with SOC. In contrast, when only cathode shrinkage is activated, the reaction force exhibits an opposite trend (Fig. 4c). By superimposing the reaction forces from the cathode and anode (Ca + An), we obtain the net contribution of electrode volume changes to the overall cell swelling (Fig. 4d). At this stage, the resulting curve already resembles the full-cell-scale swelling behavior, although the magnitude of the swelling force is smaller. The first and second peaks reach 124 N and 98 N, respectively. These values represent only the internal contributions arising from electrode volume changes. The external constraint is another critical contributor to the total swelling force, but it typically provides a constant baseline through preloading. When neither cathode nor anode volume

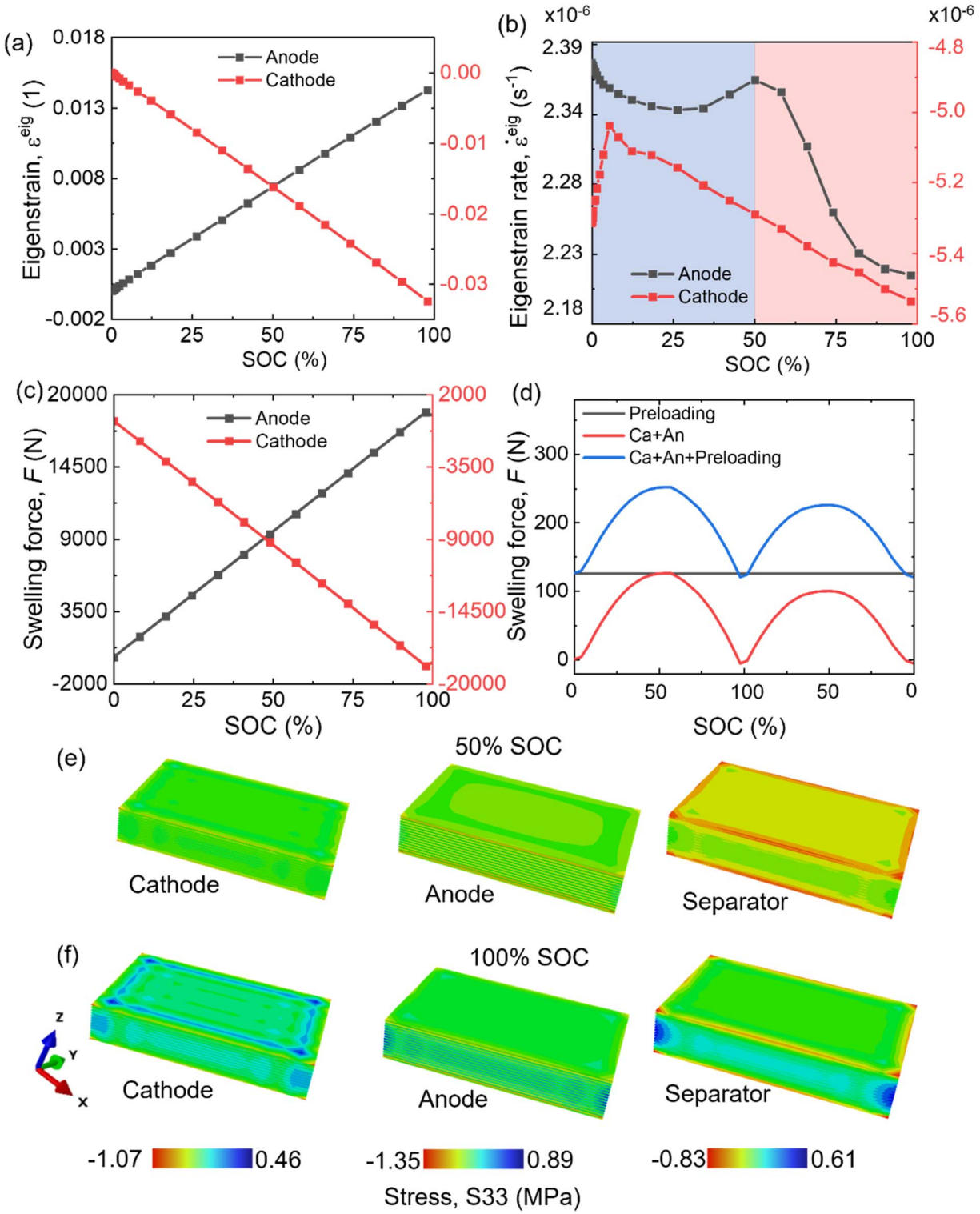

Fig. 4 Component-wise analysis of swelling contributions in sodium-ion batteries (computational results). (a) Evolution of swelling eigenstrain in the anode and cathode as a function of state of charge, highlighting monotonic anode expansion and cathode shrinkage during cycling. (b) Corresponding swelling eigenstrain rates, revealing a transition in the dominant electrochemo-mechanical contribution around 50% SOC, with anode expansion dominating at low SOC and cathode shrinkage becoming increasingly influential at high SOC. (c) Single-electrode cases only: swelling force when considering anode expansion (anode) alone or cathode contraction (cathode) alone, highlighting their independent SOC-dependent contributions. (d) Combined effects: swelling force under external mechanical preloading only (preloading), electrode contributions combined (Ca + An), and the superposition of both mechanisms (Ca + An + preloading), illustrating the joint impact of mechanical constraint and electrode volume-change effects across SOC. (e and f) Distributions of the through-thickness normal stress S33 in the cathode, anode, and separator at (c) 50% SOC and (d) 100% SOC extracted from the three-dimensional electrochemo-mechanical model. The stress contours illustrate the SOC-dependent redistribution of internal load among individual components, linking particle-level volumetric evolution to macroscopic swelling force generation.

change is considered, the baseline force can be directly obtained and is 126.2 N. Finally, by combining this baseline preloading force with the electrode contributions (Ca + An + preloading), the complete swelling force curve of the cell is recovered.

The normal stress in the thickness (z) direction, S_{33}, is used as a metric to quantify the magnitude of the internal swelling stress of the cell under stack pressure. At 50% SOC, the cathode, anode, and separator are all under compressive stress. Notably, the anode experiences higher compressive stress, indicating that it bears a larger portion of the load, consistent with the anode-dominated swelling behavior at this state. The separator primarily serves as a load-transfer and buffering layer; however, the outermost separator still carries a relatively high stress because the stack pressure is directly applied to it (Fig. 4c). At the fully charged state, the stresses in the anode and the outermost separator, which previously bore most of the load, are significantly reduced. This reduction is mainly attributed to cathode-dominated shrinkage, which helps alleviate the mechanical load on the other components (Fig. 4d). In addition, pronounced edge effects are observed in the separator, indicating stronger contact-pressure gradients and enhanced load transfer in the thickness direction near the boundaries under stack pressure (Fig. 4c and d).

3.3 SOC-dependent dominant swelling mechanisms

During charging, the volume evolution of cathode and anode particles at different SOCs, together with their interactions with internal components, governs the distinctive bimodal swelling behavior of sodium-ion batteries under stack pressure. The fixed constraints imposed on the top and bottom boundaries provides the external mechanical confinement experienced by the cell, preventing free relaxation of electrode particle volume changes and instead converting them into internal contact stresses and macroscopic swelling force (Fig. 1b). The external constraint contributes a constant baseline to the overall swelling force (Fig. 4d). At 0% SOC, both cathode and anode particles remain at their initial sizes, with particle–particle and electrode-separator contacts established but without the development of significant internal stress. As charging proceeds to approximately 50% SOC, the HC anode particles undergo continuous expansion at a rate exceeding the shrinkage rate of the NNMF cathode electrode (Fig. 4b). This also leads to competing reaction forces originating from the cathode and anode (Fig. 4c). Consequently, particle–particle and electrode–separator contacts are enhanced, causing the separator to shift toward the cathode side and leading to the establishment of internal stress (Fig. 4e). This anode-expansion-dominated regime results in a rising swelling force, which reaches its peak at 50% SOC (Fig. 5).

As charging continues to full capacity, the anode keeps expanding while the cathode continues to shrink; however, the cathode electrode shrinkage becomes more pronounced (Fig. 4b). This is because O3-type layered oxide cathodes typically undergo multistep phase transitions during deep desodiation and may exhibit substantial overall volume change,

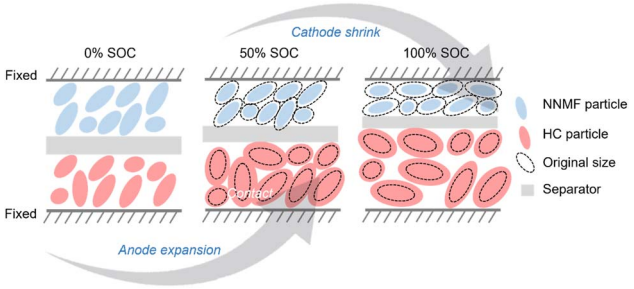

Fig. 5 Stage-dependent dominant swelling mechanisms under through-thickness constraint. Schematic illustration of particle-scale deformation and contact evolution at different states of charge. At low to intermediate SOC (0–50% SOC), volumetric expansion of anode active particles dominates the electrochemo-mechanical response, leading to enhanced particle–particle contact and a progressive increase in swelling force under fixed boundary conditions. As SOC increases further (50–100% SOC), cathode active particle shrinkage becomes the dominant mechanism, altering the internal contact state and governing the subsequent evolution of the swelling force. Dashed outlines indicate the original particle size, highlighting the asymmetric and stage-dependent contributions of the anode and cathode to the coupled electrochemo-mechanical behavior.

with contraction often becoming more pronounced in the high SOC region.[73,74] Meanwhile, sodium storage in hard carbon at high SOC is mainly dominated by pore filling, which produces much less electrode-level strain than the earlier sodiation processes associated with greater structural expansion.[67,68] Therefore, at high SOC, cathode shrinkage can become sufficiently significant to compete with anode expansion in determining the overall cell-level thickness change. As a result, contact-induced internal stresses are progressively relieved, and the separator continues to shift toward the cathode side (Fig. 4f). At this stage, the cumulative shrinkage of the cathode becomes sufficient to offset the net thickness increase induced by the anode and further reduce the overall cell thickness, thereby reversing the trend of the macroscopic reaction force. This cathode-shrinkage-dominated stage is manifested as a decrease in the macroscopic swelling force. Such SOC-dependent swelling mechanisms highlight the strong electrochemo-mechanical coupling inherent to sodium-ion batteries. Fig. 5 provides a schematic for microstructural interpretation of the SOC-dependent force contribution shift identified by the component-resolved analysis.

This feature may also be qualitatively relevant beyond the specific chemistry studied here. For layered sodium-ion oxide cathodes, not only O3-type materials but also high-voltage transitions such as P2 → O2/OP4 (ref. 75) and P3 → O3 (ref. 76) can lead to significant volume changes, often accompanied by cathode contraction. Therefore, a similar competition between cathode shrinkage and anode expansion may also occur in other layered oxide/hard-carbon sodium-ion systems. However, the quantitative magnitude of this competition remains strongly chemistry-dependent, since it is governed by the specific cathode composition, phase-transition pathway, and the pore-structure-dominated sodiation behavior of the hard carbon anode.

4 Influence of charging rate on electrochemo-mechanical coupled swelling

Due to the known limitations of the Newman model in accurately capturing high-C-rate electrochemical behavior,[77–80] the discussion is limited to the range of 0.1–1.0C. In terms of electrochemical response, higher C-rates result in higher operating voltages and earlier termination of the charging process due to enhanced polarization effects (Fig. 6a). At different C-rates, sodium-ion batteries consistently exhibit bimodal swelling behavior with comparable peak magnitudes. However, as the C-rate increases, the swelling force at the end of charging increases and occurs earlier, reaching 97 N, 111 N, and 127 N at 0.1, 0.5, and 1.0C, respectively. And the swelling-force peak during discharge also shifts noticeably toward earlier times (Fig. 6a). This behavior primarily arises from increased overpotential at higher C-rates, which causes the cutoff voltage to be reached earlier (Fig. 6d and e). At a high charging rate, the increased overpotential enhances polarization and causes the interfacial reaction kinetics to outpace solid-state diffusion more strongly. Consequently, sodium-ion insertion/extraction becomes increasingly localized near the particle surface, generating steeper intraparticle concentration gradients. Such

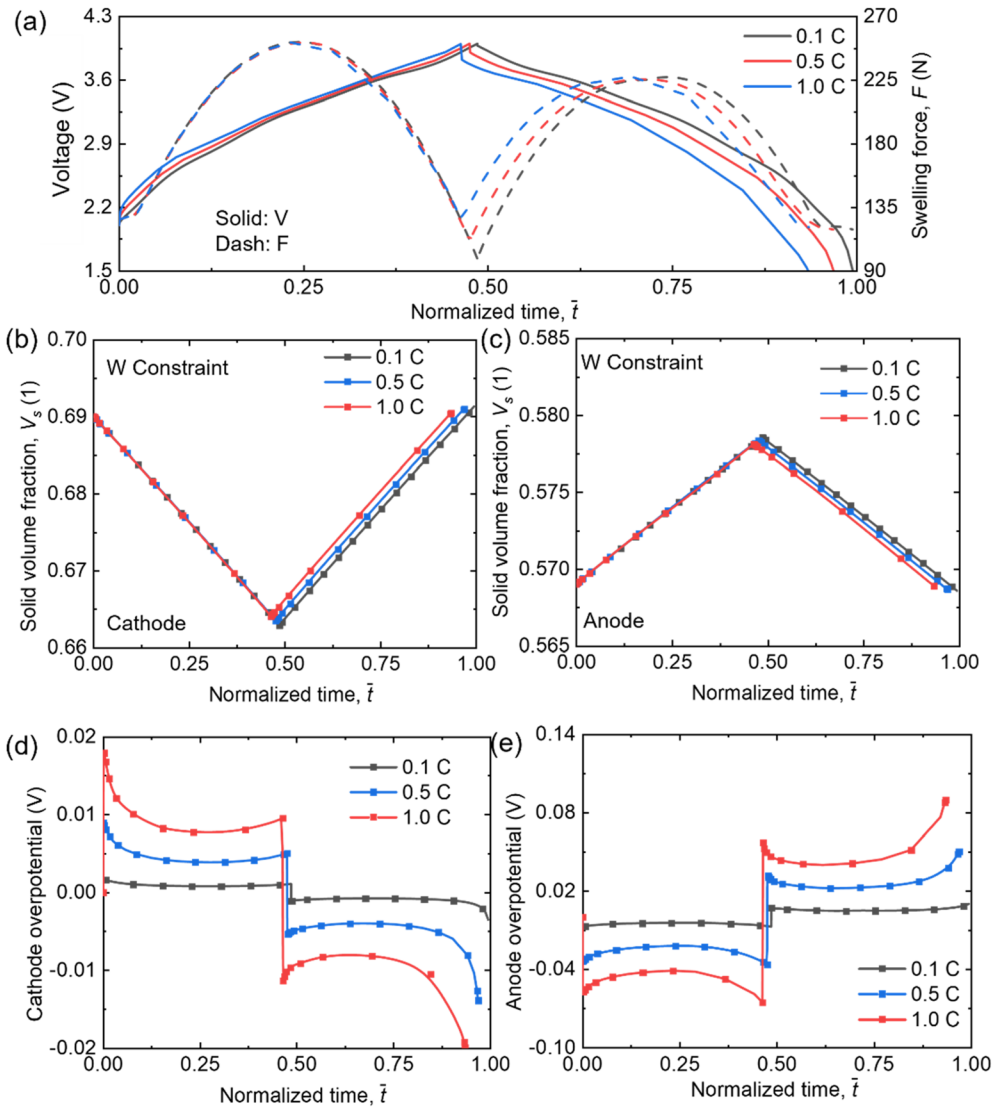

Fig. 6 Influence of charging rate on electrochemo-mechanical coupled swelling behavior (computational results). (a) Coupled voltage and swelling force responses at different charging rates (0.1C, 0.5C, and 1.0C) under through-thickness constraint. Solid lines denote voltage evolution, while dashed lines represent the corresponding swelling force. Evolution of solid volume fraction in the cathode (b) and anode (c), respectively, highlighting rate-dependent changes in electrochemically induced volumetric deformation under mechanical constraint. Cathode (d) and anode (e) overpotentials as functions of normalized time for different charging rates, illustrating the increased polarization and asymmetric electrochemical response at higher rates. These results demonstrate that increasing the charging rate amplifies electrochemo-mechanical coupling, modifies the temporal evolution of swelling force, and contributes to the emergence of rate-dependent swelling characteristics. For ease of comparison, all results are normalized by the cycle time at 0.1C.

kinetic heterogeneity leads to more pronounced surface-localized eigenstrain and a larger internal chemo-mechanical mismatch, which can contribute to the increased swelling force observed at the end of charge. In addition, near full charge, the shrinkage rate of cathode particles continues to increase, whereas the expansion rate of anode particles progressively decreases (Fig. 4b), further magnifying the difference in the cell-level swelling force under high-rate charging.

Under stack pressure, the swelling-shrinkage behavior of the cell primarily induces changes in the solid volume fraction of the electrodes, including contributions from active particles. During charging, the cathode exhibits shrinkage, leading to a decrease in solid volume fraction, whereas the anode undergoes expansion, resulting in an increase in solid volume fraction; the opposite trend is observed during discharge, and the variations are approximately linear. The initial solid volume fraction of the cathode is 0.69 and decreases to 0.662, 0.663, and 0.664 at 0.1C, 0.5C, and 1.0C, respectively (Fig. 6b). In contrast, the anode shows a smaller change, with the solid volume fraction increasing from 0.569 to 0.5785, 0.5783, and 0.5781 at the corresponding C-rates (Fig. 6c). Lower C-rates allow more extensive sodium-ion deintercalation and intercalation, leading to larger changes in solid volume fraction. As the C-rate increases from 0.1 to 1.0C, the overpotentials of both cathode and anode increase, indicating enhanced polarization at higher C-rates. The anode exhibits a larger overall overpotential, suggesting it contributes more significantly to the total polarization (Fig. 6d and e).

5 Concluding remarks

Understanding the electrochemo-mechanical coupling in sodium-ion batteries and the mechanisms underlying it is critical for enhancing safety and optimizing electrochemical performance. This study aims to elucidate the electrochemo-mechanically coupled swelling behavior of sodium-ion batteries and the underlying physical mechanisms. *Operando* swelling-force measurements are conducted to directly capture the dynamic swelling response during electrochemical cycling. To interpret the origin of the measured swelling force and to quantitatively resolve the contributions from individual cell components, a detailed, multiscale, electrochemo-mechanical coupled computational framework is developed and rigorously validated against experimental data. The influence of C-rate on coupled swelling behavior is systematically examined. Based on these combined experimental and modeling insights, an SOC-dependent, stage-wise electrode-dominated swelling mechanism is established.

(1) *Operando* swelling-force measurements reveal a unique bimodal swelling behavior in sodium-ion batteries. During charge and discharge, a pronounced swelling peak consistently appears at approximately 50% SOC, with a higher peak during charging.

(2) The underlying mechanism of the bimodal swelling behavior arises from the competition between anode and cathode volume (eigenstrain) changes. In the low-SOC regime (0–50% SOC), the swelling force is predominantly governed by anode-dominated expansion. In contrast, in the high-SOC regime (50–100% SOC), cathode-dominated shrinkage reduces the swelling force. The separator primarily functions as a load-transfer and mechanical buffering layer.

(3) At higher C-rates, the swelling force at the fully charged state increases, and the peak swelling force during discharge occurs earlier, driven by enhanced overpotential and accelerated ionic (de)intercalations. These results highlight the strong electrochemo-mechanical coupling underlying the swelling behavior.

By integrating *operando* observations with an advanced computational framework, this work provides an in-depth understanding of the unique electrochemo-mechanical coupled swelling behavior of sodium-ion batteries. The combined experimental and computational insights establish a solid foundation and offer practical guidance for the commercialization of sodium-ion batteries and the design of next-generation SIB systems.

Author contributions

Bo Rui: writing – original draft, methodology, investigation, formal analysis, data curation. Youngwon Hahn: methodology. Amit Bhowmick: experiment, investigation. Farzaneh Mousavi: methodology. Sandeep Kulathu: writing – review & editing. Victor Oancea: writing – review & editing. Jun Xu: conceptualization, methodology, supervision, and writing – review & editing.

Conflicts of interest

The authors declare that they have no known competing financial interests or personal relationships that could have appeared to influence the work reported in this paper.

Nomenclature

F^1_{Peak}	Peak force during charge (N)
F^2_{Peak}	Peak force during discharge (N)
ΔF	Force difference of peak force during discharge and charge (N)
a	Specific surface area of active particle (m^{-1})
c	Concentration (mol m^{-3})
D	Diffusion coefficient (m^2 s^{-1})
E	Young's modulus (MPa)
F	Faraday's constant (9.64853×10^4 C mol^{-1})
I	Current (A)
i	Current density (A m^{-2})
j_0	Exchange current density (A m^{-2})
j_{loc}	Local current density (A m^{-2})
k^c	Rate constant of cathode (m s^{-1})
k^a	Rate constant of anode (m s^{-1})
R_g	Universal gas constant, 8.314 (J $(mol\ K)^{-1}$)
R	Resistance (Ω)
r	Particle radius (m)
t	Time (s)

$t-$	Normalized time (1)
$t+$	Transference number (1)
T	Temperature (°C)
V	Voltage (V)
t^{j}	Thickness of jellyroll (m)
w^{j}	Width of jellyroll (m)
$\mathbf{D}^{el}$	Constitutive relation matrix
$\mathbf{b}$	Body force per unit volume (N m^{-3})
S_{33}	Normal stress in the thickness (z) direction (MPa)
α	Conversion degree (1)
ν	Poisson's ratio (1)
ε	Strain (1)
ε_e	Volume fraction (1)
ρ	Density (kg m^{-3})
ϕ	Potential (V)
φ	Efficacy coefficient (1)
η	Overpotential (V)
κ	Electrical conductivity (S m^{-1})
δ	Thickness of 3D model (m)
ε^{el}	Elastic strain (1)
ε^{eig}	Eigenstrain (1)
0	Initial state
eff	Effective property
e	Electrolyte
s	Solid
D	Diffusion
c	Cathode
a	Anode
se	Separator
j	Jellyroll
eq	Equilibrium
pc	Cathode current collector
nc	Anode current collector
ps	Cathode active layer
ng	Anode active layer
Al	Aluminum

Data availability

The data supporting this article have been included as part of the supplementary information (SI). Supplementary information is available. See DOI: https://doi.org/10.1039/d6ta01576j.

Acknowledgements

J. X. appreciates the financial support from the University of Delaware startup funding, NASA EPSCoR, and the research project with Dassault Systèmes.

References

1 N. Yabuuchi, K. Kubota, M. Dahbi and S. Komaba, *Chem. Rev.*, 2014, **114**, 11636–11682.
2 C. Vaalma, D. Buchholz, M. Weil and S. Passerini, *Nat. Rev. Mater.*, 2018, **3**, 18013.
3 A. Yao, S. M. Benson and W. C. Chueh, *Nat. Energy*, 2025, **10**, 404–416.
4 L. Yang, X. Yin, J. Wang, Y. Sun, Y. Li, Z. Zhang, Z. Liu, S.-M. Huang, P. Adelhelm and D. Zhou, *Nat. Rev. Chem.*, 2026, 1–16.
5 Z. Gao, S. Yang, R. Chen, Y. Ding, S. Guo, S. Zhan, B. Cui, J. Zheng, T. Liu, H. Luo and M. Lu, *Adv. Funct. Mater.*, 2026, **36**, e07323.
6 F. Zhang, B. He, Y. Xin, T. Zhu, Y. Zhang, S. Wang, W. Li, Y. Yang and H. Tian, *Chem. Rev.*, 2024, **124**, 4778–4821.
7 B. Rui, S. Sun, X. Tan, C. (Michael) Chak, L. Ma and J. Xu, *J. Mater. Chem. A*, 2025, **13**, 12203–12215.
8 J.-Y. Hwang, S.-T. Myung and Y.-K. Sun, *Chem. Soc. Rev.*, 2017, **46**, 3529–3614.
9 Z. Zhang, D. Zhao, Y. Xu, S. Liu, X. Xu, J. Zhou, F. Gao, H. Tang, Z. Wang, Y. Wu, X. Liu and Y. Zhang, *Chem. Rec.*, 2022, **22**, e202200127.
10 Q. Li, H. Liu, Y. Ye, K. J. Li, F. Wu, L. Li and R. Chen, *Nat. Energy*, 2025, **10**, 1064–1073.
11 M.-T. F. Rodrigues, G. Babu, H. Gullapalli, K. Kalaga, F. N. Sayed, K. Kato, J. Joyner and P. M. Ajayan, *Nat. Energy*, 2017, **2**, 17108.
12 C. Yuan, Y. Hahn, W. Lu, V. Oancea and J. Xu, *Cell Rep. Phys. Sci.*, 2022, **3**, 101158.
13 S. Sun, B. Rui, S. Bahuguna, J. Zhou, F. Sayeed and J. Xu, *Energy Storage Mater.*, 2026, 105022.
14 Y. Cao, H. Wang, B. Liu and J. Xu, *J. Energy Storage*, 2023, **74**, 109499.
15 Y. K. Lee, C. Sung, J. Kim, C. Hong and J. Choi, *J. Energy Storage*, 2024, **82**, 110431.
16 B. Özdogru, H. Dykes, S. Padwal, S. Harimkar and Ö. Ö. Çapraz, *Electrochim. Acta*, 2020, **353**, 136594.
17 L. Wang, Y. Chen, G. Jia, Y. Cui, X. Zhao, L. Liu, X. Han and Y. Wang, *J. Energy Storage*, 2026, **141**, 119245.
18 V. A. Sethuraman, M. J. Chon, M. Shimshak, V. Srinivasan and P. R. Guduru, *J. Power Sources*, 2010, **195**, 5062–5066.
19 J. Cannarella and C. B. Arnold, *J. Power Sources*, 2014, **245**, 745–751.
20 J. Christensen and J. Newman, *J. Solid State Electrochem.*, 2006, **10**, 293–319.
21 B. Rieger, S. Schlueter, S. V. Erhard, J. Schmalz, G. Reinhart and A. Jossen, *J. Energy Storage*, 2016, **6**, 213–221.
22 H. Aziam, G. Garhi, Y. Tamraoui, L. Ma, T. Wu, G. L. Xu, B. Manoun, J. Alami, K. Amine and I. Saadoune, *Electrochim. Acta*, 2018, **283**, 1238–1244.
23 M. T. McDowell, S. W. Lee, J. T. Harris, B. A. Korgel, C. Wang, W. D. Nix and Y. Cui, *Nano Lett.*, 2013, **13**, 758–764.
24 M. N. Obrovac, *Curr. Opin. Electrochem.*, 2018, **9**, 8–17.
25 B. Rui, B. Lu, Y. Song and J. Zhang, *Appl. Math. Mech.*, 2023, **44**, 547–560.
26 L. Cheng, Q. Xiao, W. Li, M. Yu, M. Xiao, D. Peng, D. Zhang and Z. Xing, *J. Colloid Interface Sci.*, 2026, **708**, 139759.
27 L. Yin, W. Li, Q. Cao, S. W. Or and Z. Xing, *Chem*, 2024, **10**, 2609–2614.
28 S. Waluś, G. Offer, I. Hunt, Y. Patel, T. Stockley, J. Williams and R. Purkayastha, *Energy Storage Mater.*, 2018, **10**, 233–245.

29 A. Durdel, J. Brehm, V. Elender, L. Bitschnau, A. Aufschläger, M. Altmann, P. Kotter and A. Jossen, *J. Electrochem. Soc.*, 2025, **172**, 050508.
30 D. Vidal, C. Leys, B. Mathieu, N. Guillet, V. Vidal, D. Borschneck, P. Chaurand, S. Genies, E. De Vito, M. Tulodziecki and W. Porcher, *J. Power Sources*, 2021, **514**, 230552.
31 H. Wang, Y. Wu, Y. Cao, M. Liu, X. Liu, Y. Liu and B. Liu, *iScience*, 2024, **27**, 111300.
32 J. L. Gómez-Cámer, C. Bünzli, M. M. Hantel, T. Poux and P. Novák, *Carbon*, 2016, **105**, 42–51.
33 I. Escher, Y. Kravets, G. A. Ferrero, M. Goktas and P. Adelhelm, *Energy Technol.*, 2021, **9**, 2000880.
34 A. M. Stavola, X. Sun, D. P. Guida, A. M. Bruck, D. Cao, J. S. Okasinski, A. C. Chuang, H. Zhu and J. W. Gallaway, *ACS Energy Lett.*, 2023, **8**, 1273–1280.
35 A. Torayev, S. Engelke, Z. Su, L. E. Marbella, V. De Andrade, A. Demortière, P. C. M. M. Magusin, C. Merlet, A. A. Franco and C. P. Grey, *J. Phys. Chem. C*, 2021, **125**, 4955–4967.
36 D. Sauerteig, N. Hanselmann, A. Arzberger, H. Reinshagen, S. Ivanov and A. Bund, *J. Power Sources*, 2018, **378**, 235–247.
37 Y. Orikasa, Y. Gogyo, H. Yamashige, M. Katayama, K. Chen, T. Mori, K. Yamamoto, T. Masese, Y. Inada, T. Ohta, Z. Siroma, S. Kato, H. Kinoshita, H. Arai, Z. Ogumi and Y. Uchimoto, *Sci. Rep.*, 2016, **6**, 26382.
38 M. Ender, A. Weber and E. Ivers-Tiffée, *Electrochem. Commun.*, 2013, **34**, 130–133.
39 P. Pietsch, D. Westhoff, J. Feinauer, J. Eller, F. Marone, M. Stampanoni, V. Schmidt and V. Wood, *Nat. Commun.*, 2016, **7**, 12909.
40 Z. Stravova, O. Klvac, J. Bana, B. Anothumakkool, T. Zikmund, P. Blazek, J. Kaiser and T. Kazda, *Sci. Rep.*, 2024, **14**, 28546.
41 P. Daubinger, M. Schelter, R. Petersohn, F. Nagler, S. Hartmann, M. Herrmann and G. A. Giffin, *Adv. Energy Mater.*, 2022, **12**, 2102448.
42 W. Li, J. Jiao, R. C. Ihuaenyi, K. Karch, C. Cater and J. Zhu, *J. Electrochem. Energy Convers. Storage*, 2026, **23**, 021005.
43 P. Blažek, O. Klvač, M. Šedina, O. Čech, M. Tkadlecová, Z. Stravová, T. Kazda, T. Zikmund, R. H. Schmitt and J. Kaiser, *J. Energy Storage*, 2025, **130**, 117436.
44 M. Spielbauer, J. Soellner, P. Berg, K. Koch, P. Keil, C. Rosenmüller, O. Bohlen and A. Jossen, *J. Energy Storage*, 2022, **55**, 105564.
45 J. Xu, B. Liu and D. Hu, *Sci. Rep.*, 2016, **6**, 1–11.
46 K.-Y. Oh and B. I. Epureanu, *J. Power Sources*, 2016, **303**, 86–96.
47 P. K. Leung, C. Moreno, I. Masters, S. Hazra, B. Conde, M. R. Mohamed, R. J. Dashwood and R. Bhagat, *J. Power Sources*, 2014, **271**, 82–86.
48 P. Höschele, S. F. Heindl, S. Erker and C. Ellersdorfer, *J. Energy Storage*, 2023, **65**, 107228.
49 A. Leonard, B. Planden, K. Lukow and D. Morrey, *J. Energy Storage*, 2023, **72**, 108422.
50 N. A. Samad, Y. Kim, J. B. Siegel and A. G. Stefanopoulou, *J. Electrochem. Soc.*, 2016, **163**(8), A1584–A1594.
51 Y. Li, C. Wei, Y. Sheng, F. Jiao and K. Wu, *Ind. Eng. Chem. Res.*, 2020, **59**, 12313–12318.
52 A. J. Louli, L. D. Ellis and J. R. Dahn, *Joule*, 2019, **3**, 745–761.
53 C. Jin, Y. Wang, A. S. Borujerdi and J. Li, *J. Power Sources Adv.*, 2022, **16**, 100103.
54 S. Niu, S. Heng, G. Zhu, J. Xu, Q. Qu, K. Wu and H. Zheng, *J. Energy Storage*, 2021, **44**, 103425.
55 J. Cannarella and C. B. Arnold, *J. Power Sources*, 2014, **269**, 7–14.
56 D. Sauerteig, S. Ivanov, H. Reinshagen and A. Bund, *J. Power Sources*, 2017, **342**, 939–946.
57 W. Li, X. Wu, K. Wang, M. Ling, Z. Lin, M. Wang, H. Sun, K. Wu and C. Liang, *J. Power Sources*, 2024, **622**, 235330.
58 A. Bhowmick, B. Rui, S. Sun, X. Tan, B. Wei, Y. Hahn, S. Kulathu, V. Oancea, W. Lu and J. Xu, *Nano Energy*, 2026, **150**, 111751.
59 C. Tealdi, J. Heath and M. S. Islam, *J. Mater. Chem. A*, 2016, **4**, 6998–7004.
60 B. Özdogru, H. Dykes, D. Gregory, D. Saurel, V. Murugesan, M. Casas-Cabanas and Ö. Ö. Çapraz, *J. Power Sources*, 2021, **507**, 230297.
61 M. Wable, B. Bal and Ö. Ö. Capraz, *Energy Adv.*, 2024, **3**, 601–608.
62 *Abaqus Analysis User's Guide. Version 2026*, Dassault Systémes Simulia Corp, 2026.
63 M. Doyle, J. Newman, A. S. Gozdz, C. N. Schmutz and J.-M. Tarascon, *J. Electrochem. Soc.*, 1996, **143**, 1890.
64 M. Doyle, T. F. Fuller and J. Newman, *J. Electrochem. Soc.*, 1993, **140**, 1526–1533.
65 M. Doyle and J. Newman, *Electrochim. Acta*, 1995, **40**, 2191–2196.
66 S. Kulathu, J. A. Hurtado, K. Bose, Y. Hahn, P. A. Bouzinov, R. L. Taylor and V. Oancea, *Int. J. Numer. Methods Eng.*, 2024, **125**, e7464.
67 E. M. Reynolds, J. Fitzpatrick, M. O. Jones, N. Tapia-Ruiz, H. Y. Playford, S. Hull, I. McClelland, P. J. Baker, S. A. Cussen and G. E. Pérez, *J. Mater. Chem. A*, 2024, **12**, 18469–18475.
68 Y. Morikawa, S. Nishimura, R. Hashimoto, M. Ohnuma and A. Yamada, *Adv. Energy Mater.*, 2020, **10**, 1903176.
69 A. Chanda, A. Pakhare, A. Alfadhli, V. A. Sethuraman and S. P. V. Nadimpalli, *J. Power Sources*, 2024, **609**, 234678.
70 Y. Xie, H. Wang, G. Xu, J. Wang, H. Sheng, Z. Chen, Y. Ren, C.-J. Sun, J. Wen, J. Wang, D. J. Miller, J. Lu, K. Amine and Z.-F. Ma, *Adv. Energy Mater.*, 2016, **6**, 1601306.
71 A. Chanda, D. P. Abraham, S. E. Trask and S. P. V. Nadimpalli, *EES Batter.*, 2025, **1**, 833–839.
72 E. Song, B. L. Nelson and J. Staum, *SIAM/ASA J. Uncertain. Quantif.*, 2016, **4**, 1060–1083.
73 Z. Xu, H. Yang, X. Zhao, R. Zheng, Z. Song, Z. Wang, H. Sun, Y. Liu and D. Wang, *ACS Appl. Mater. Interfaces*, 2025, **17**, 1085–1096.
74 M. Li, H. Zhuo, J. Lei, Y. Guo, Y. Yuan, K. Wang, Z. Liao, W. Xia, D. Geng, X. Sun, J. Hu and B. Xiao, *Nat. Commun.*, 2025, **16**, 2010.
75 P. Hou, Z. Lin, M. Dong, Z. Sun, M. Gong, F. Li and X. Xu, *J. Colloid Interface Sci.*, 2023, **649**, 1006–1013.

76 Y. Shi, Z. Zhang, P. Jiang, A. Gao, K. Li, Q. Zhang, Y. Sun, X. Lu, D. Cao and X. Lu, *Energy Storage Mater.*, 2021, **37**, 354–362.
77 A. A. Franco, A. Rucci, D. Brandell, C. Frayret, M. Gaberscek, P. Jankowski and P. Johansson, *Chem. Rev.*, 2019, **119**, 4569–4627.
78 X. Duan, D. Hu, W. Chen, J. Li, L. Wang, S. Sun and J. Xu, *Adv. Energy Mater.*, 2024, 2400710.
79 G. Richardson, G. Denuault and C. P. Please, *J. Eng. Math.*, 2012, **72**, 41–72.
80 S. Santhanagopalan, Q. Guo, P. Ramadass and R. E. White, *J. Power Sources*, 2006, **156**, 620–628.